SI Appendix

Chemical intermixing

The EELS line profiles in supplementary Fig. S3 and S4 show that for $N = 10$ and $N = 32$ u.c., the LSMO blocks both start with and terminate with an (LaSr)O layer. Similar with the $N = 4$ u.c. superlattice, the A-site intermixing between LaSr and Ba is confined within one layer.

Magnetization

The magnetization vs. temperature and field curves are shown in Figs. S6 and S7. The relatively thick $N = 32$ u.c. film shows a clear paramagnetic to ferromagnetic transition above room temperature and strong ferromagnetism at 10 K. As the LSMO thickness is reduced, ferromagnetism is strongly quenched and nearly disappears around $N = 6$ u.c. films. Such monotonic suppression of ferromagnetism as thickness is reduced is commonly observed. Surprisingly, the ferromagnetism reemerges for $N = 4$ and 3 u.c. with a clear paramagnetic-to-ferromagnetic transition at 172 K and 160 K and clear hysteresis behavior in the M vs. H curves. We note that in the $N = 2$ u.c. film, the intermixing at both sides of the interface may play an important role, giving rise to reduced ferromagnetism.

We also exclude the possibility of major magnetic contribution from Ti. Since the number of BTO layers are linearly increased with reducing LSMO thickness, if the Ti has magnetism, one would expect a linear increase of magnetism with reduced N, contradicting our observations. We also measured a contrast sample consisting of a $(BTO_{21}/STO_4)_{10}$ superlattice on an STO substrate, showing that both BTO and STO substrates have negligible contribution to magnetism.

Determination of Mn valence

The Mn oxidation states were determined by two methods: The Mn L_{23} ratio and the energy separation (ΔE) between the O pre-peak and the adjacent main peak. The L_{23} ratio decreases as the Mn oxidation state increases. The energy separation (ΔE) increases steadily as the Mn oxidation state increases. As shown in Figs. S10 and S11, a slight decrease of ΔE and increase in the L_{23} ratio indicate reduced Mn oxidation states near the interface. The quantitative relationship between the L_{23} ratio and ΔE with the Mn oxidation state has been reported in previous literature[1]. Furthermore, the Mn oxidation state was further calibrated by a standard LSMO sample. The Mn oxidation states determined by the Mn L_{23} ratio and the O ΔE are consistent with each other.

The Mn *L* edge results from excitations of 2*p* electrons into empty 3*d/3s* states and the continuum. The L_3 edge corresponds to the 2*p* 3/2 to 3*d/3s* excitation, and the L_2 edge is attributed to the 2*p* 1/2 to 3*d/3s* excitation. The electron configuration is $t_{2g}^3\ e_g^1$ for Mn^{4+}, and $t_{2g}^3\ e_g^0$ for Mn^{3+}. In general, the Mn oxidation states in LSMO can be considered as a mixture of Mn^{4+} and Mn^{3+}. The intensity ratio of L_3 to L_2 edges decreases as the oxidation state of Mn increase from 3+ to 4+.

The O *K* edge results from excitations of O *1s* electrons into *2p* states. Three featured peaks are shown in the near-edge fine structure of the O-*K* edge. The first peak is the pre-peak, and it has strong hybridization with Mn *3d* states. Since the t_{2g} band of LMSO if fully occupied, the pre-peak has a very strong contribution from the Mn *3d* e_g band, i.e. we can get information about the Mn *3d* band occupancy (Mn oxidation states) from it. The second and third peak are the main peaks, which are attributed to hybridization with La *5d*/Sr *3d* bands (first main peak) and the Mn 4*sp* (second main peak) band, separately. The energy separation (ΔE) between the pre-peak and

the adjacent main peak increases with increasing Mn oxidation states. This dependence is attributed to a chemical-potential shift of the initial core and the final states of the ejected electron.

Bond Angle Calculation

As shown in Fig. 2, we have directly measured the in-plane $\delta_{Mn\text{-}O}$ displacement along the [110] direction. One can straightforwardly derive the corresponding Mn-O-Mn in-plane (IP) bond angle Θ_{IP} in the (110) plane and project it back 45 degrees to obtain the real values of the IP bond angle in the (100) plane, as the data shown in Fig. 6a.

The out-of-plane (OP) bond angle Θ_{OP}, on the other hand, is difficult to measure directly because of the large size of La/Sr atoms located on top of the oxygen connecting each layer, as shown in red lines in Fig. S13. In the assumption of rigid octahedron tilt, the IP bond angle in the (110) projected plane is equal to the OP bond angle and both should be uniform for each layer. In N = 10 u.c. films (Fig. 2b), the atomically-resolved layer-by-layer difference of IP bond angles suggests that the octahedrons slightly lose their rigidity. Therefore, in order to calculate the OP bond angle values for each interlayer, we average the IP bond angles in the (110) projected plane from its two neighboring layers. The results are shown in Fig. 6b. Such approximation does not change the physics and qualitative conclusion of our Monte-Carlo simulation. In the N = 4 u.c. film, like BTO, the OP bond angle is simply set to be 180 degrees due to its polar nature.

Monte Carlo simulation on double-exchange model

The two-orbital double-exchange model is a well-accepted canonical model to describe the magnetic phases in manganites[2,3]. The model Hamiltonian reads:

$$H=\sum_{<ij>,\alpha\beta}t^{\vec{r}}_{\alpha\beta}(\Omega_{ij}c^{+}_{i,\alpha}c_{j,\beta}+h.c.)+\sum_{<ij>}J^{\vec{r}}_{AF}\vec{S}_i\cdot\vec{S}_j+\lambda\sum_i(-Q_{1,i}n_i+Q_{2,i}\tau^x_i+Q_{3,i}\tau^y_i)+\sum_i(2Q^2_{1,i}+Q^2_{2,i}+Q^2_{3,i}), \quad (1)$$

where the first term denotes the double-exchange hopping between orbitals α and β of nearest-neighbor (NN) sites *i* and *j*. The hopping amplitude *t* depends on both the orbitals and directions, as well as the bond angle[4,5].

$$t^x=\begin{pmatrix}t^x_{aa} & t^x_{ab}\\ t^x_{ba} & t^x_{bb}\end{pmatrix}=\frac{t_0}{4}\begin{pmatrix}3\cos^3\Phi^{xy} & \sqrt{3}\cos^2\Phi^{xy}\\ \sqrt{3}\cos^2\Phi^{xy} & \cos\Phi^{xy}\end{pmatrix}, \quad (2)$$

$$t^y=\begin{pmatrix}t^y_{aa} & t^y_{ab}\\ t^y_{ba} & t^y_{bb}\end{pmatrix}=\frac{t_0}{4}\begin{pmatrix}3\cos^3\Phi^{xy} & -\sqrt{3}\cos^2\Phi^{xy}\\ -\sqrt{3}\cos^2\Phi^{xy} & \cos\Phi^{xy}\end{pmatrix}, \quad (3)$$

$$t^z=\begin{pmatrix}t^z_{aa} & t^z_{ab}\\ t^z_{ba} & t^z_{bb}\end{pmatrix}=\frac{t_0}{16}\begin{pmatrix}0 & 0\\ 0 & \cos\Phi^z(3\cos\Phi^z-1)^2\end{pmatrix}. \quad (4)$$

Here Φ_{xy} and Φ_z denote the in-plane and out-of-plane Mn-O-Mn bond angles, respectively. As a well-accepted approximation, the infinite Hund coupling gives rise to the Berry phase item $\Omega=\cos(\theta_i)\cos(\theta_j)+\cos(\theta_i)\cos(\theta_j)\exp[-(\phi-\phi_j)]$, where θ and ϕ are the polar and azimuthal angles of spin S, respectively. t_0 is taken as the energy unit in our calculation and is about 0.4-0.5 eV according to previous literature as well as the density-functional theory fitting.

The second term is the Heisenberg-type superexchange between NN spins. The exchange coefficient J_{AF} is also bond angle dependent[6]:

$$J^{\vec{r}}_{AF}=J^0_{AF}\sin^4(\frac{\Phi^{\vec{r}}}{2}), \quad (5)$$

where the superscript *r* can be either *xy* or *z*. The third term is the electron-lattice coupling with a dimensionless coefficient λ. Q_1 is the breathing mode, coupled with the local e_g density *n*. Q_2 and

Q_3 are two Jahn-Teller modes, coupled with the pseudo-spin orbital operators τ^x and τ^y, respectively. The last item is the elastic energy of lattice distortion. The definition of Q and τ can be found in Ref. [2,3].

In our simulation, J_{AF}^0 is chosen as 0.095 and λ is set as 1.2, which are reasonable values to describe $La_{1-x}Sr_xMnO_3$ according to previous literature (7,8). The lattice is $4\times4\times N$. For exchanges, the boundary conditions are periodic in the x-y plane but open along the z-axis to simulate the isolated manganite layers, while for lattice distortions, fully periodic boundary conditions are imposed since the oxygen octahedra are all complete in the superlattices. During the simulation, the average e_g density is kept to be 2/3, to exclude the influence of electron density.

Structural information for DFT calculations

- **Initial Structure of 8/4 SL with Q_{Polar} Distortion in VASP POSCAR format:**

BTO-LSMO-8/4
1.0
5.6450000008 0.0000000000 0.0000000000
0.0000000000 5.6450000000 0.0000000000
0.0000000000 0.0000000000 49.0200004578
Ba La Ti Mn O
16 8 16 8 72
Direct
0.000000000 0.000000000 0.167472005
0.000000000 0.000000000 0.501994014
0.000000000 0.000000000 0.083449997
0.000000000 0.000000000 0.418471992
0.500000000 0.500000000 0.167472005

	0.500000000	0.500000000	0.501994014
	0.500000000	0.500000000	0.083449997
	0.500000000	0.500000000	0.418471992
	0.000000000	0.000000000	0.998665988
	0.000000000	0.000000000	0.335004985
	0.000000000	0.000000000	0.251331002
	0.000000000	0.000000000	0.585780978
	0.500000000	0.500000000	0.998665988
	0.500000000	0.500000000	0.335004985
	0.500000000	0.500000000	0.251331002
	0.500000000	0.500000000	0.585780978
Sr5	0.000000000	0.000000000	0.753552973
Sr3	0.500000000	0.500000000	0.753552973
	0.000000000	0.000000000	0.669615984
Sr6	0.000000000	0.000000000	0.837450981
Sr4	0.500000000	0.500000000	0.837450981
	0.000000000	0.000000000	0.917414010
Sr2	0.500000000	0.500000000	0.917414010
Sr1	0.500000000	0.500000000	0.669615984
	0.500000000	0.000000000	0.043048002
	0.500000000	0.000000000	0.377903998
	0.000000000	0.500000000	0.043048002
	0.000000000	0.500000000	0.377903998
	0.000000000	0.500000000	0.126725003
	0.000000000	0.500000000	0.461326003
	0.500000000	0.000000000	0.126725003
	0.500000000	0.000000000	0.461326003
	0.500000000	0.000000000	0.210721999

0.500000000	0.000000000	0.544968009
0.000000000	0.500000000	0.210721999
0.000000000	0.500000000	0.544968009
0.500000000	0.000000000	0.294349015
0.500000000	0.000000000	0.628823996
0.000000000	0.500000000	0.294349015
0.000000000	0.500000000	0.628823996
0.500000000	0.000000000	0.712791026
0.000000000	0.500000000	0.712791026
0.000000000	0.500000000	0.796814978
0.500000000	0.000000000	0.796814978
0.500000000	0.000000000	0.878480971
0.000000000	0.500000000	0.878480971
0.500000000	0.000000000	0.959644973
0.000000000	0.500000000	0.959644973
0.250000000	0.250000000	0.039781000
0.250000000	0.250000000	0.374704987
0.250000000	0.250000000	0.709504008
0.250000000	0.250000000	0.207451999
0.250000000	0.250000000	0.541786015
0.250000000	0.250000000	0.875850976
0.250000000	0.250000000	0.123420000
0.250000000	0.250000000	0.458117008
0.250000000	0.250000000	0.793416977
0.250000000	0.250000000	0.291106999
0.250000000	0.250000000	0.625606000
0.250000000	0.250000000	0.956925988
0.250000000	0.750000000	0.039781000

0.250000000	0.750000000	0.374704987
0.250000000	0.750000000	0.709504008
0.250000000	0.750000000	0.207451999
0.250000000	0.750000000	0.541786015
0.250000000	0.750000000	0.875850976
0.250000000	0.750000000	0.123420000
0.250000000	0.750000000	0.458117008
0.250000000	0.750000000	0.793416977
0.250000000	0.750000000	0.291106999
0.250000000	0.750000000	0.625606000
0.250000000	0.750000000	0.956925988
0.750000000	0.250000000	0.039781000
0.750000000	0.250000000	0.374704987
0.750000000	0.250000000	0.709504008
0.750000000	0.250000000	0.207451999
0.750000000	0.250000000	0.541786015
0.750000000	0.250000000	0.875850976
0.750000000	0.250000000	0.123420000
0.750000000	0.250000000	0.458117008
0.750000000	0.250000000	0.793416977
0.750000000	0.250000000	0.291106999
0.750000000	0.250000000	0.625606000
0.750000000	0.250000000	0.956925988
0.750000000	0.750000000	0.039781000
0.750000000	0.750000000	0.374704987
0.750000000	0.750000000	0.709504008
0.750000000	0.750000000	0.207451999
0.750000000	0.750000000	0.541786015

0.750000000	0.750000000	0.875850976
0.750000000	0.750000000	0.123420000
0.750000000	0.750000000	0.458117008
0.750000000	0.750000000	0.793416977
0.750000000	0.750000000	0.291106999
0.750000000	0.750000000	0.625606000
0.750000000	0.750000000	0.956925988
0.500000000	0.000000000	0.332309008
0.500000000	0.000000000	0.666912019
0.500000000	0.000000000	0.996056974
0.500000000	0.000000000	0.164757997
0.500000000	0.000000000	0.499305010
0.500000000	0.000000000	0.835112989
0.000000000	0.500000000	0.332309008
0.000000000	0.500000000	0.666912019
0.000000000	0.500000000	0.996056974
0.000000000	0.500000000	0.164757997
0.000000000	0.500000000	0.499305010
0.000000000	0.500000000	0.835112989
0.500000000	0.000000000	0.080863997
0.500000000	0.000000000	0.415861011
0.500000000	0.000000000	0.750856996
0.500000000	0.000000000	0.248683006
0.500000000	0.000000000	0.583028018
0.500000000	0.000000000	0.915111005
0.000000000	0.500000000	0.080863997
0.000000000	0.500000000	0.415861011
0.000000000	0.500000000	0.750856996

0.000000000 0.500000000 0.248683006

0.000000000 0.500000000 0.583028018

0.000000000 0.500000000 0.915111005

- **Initial Structure of 8/4 SL with Q_{AFD} Distortion in VASP POSCAR format:**

BTO-LSMO-8/4 (Q_{AFD})

1.0

5.6449999809 0.0000000000 0.0000000000

0.0000000000 5.6449999809 0.0000000000

0.0000000000 0.0000000000 49.0200004578

Ba La Ti Mn O

16 8 16 8 72

Direct

0.000000000 0.000000000 0.167472005

0.000000000 0.000000000 0.501994014

0.000000000 0.000000000 0.083449997

0.000000000 0.000000000 0.418471992

0.500000000 0.500000000 0.167472005

0.500000000 0.500000000 0.501994014

0.500000000 0.500000000 0.083449997

0.500000000 0.500000000 0.418471992

0.000000000 0.000000000 0.998665988

0.000000000 0.000000000 0.335004985

0.000000000 0.000000000 0.251331002

0.000000000	0.000000000	0.585780978
0.500000000	0.500000000	0.998665988
0.500000000	0.500000000	0.335004985
0.500000000	0.500000000	0.251331002
0.500000000	0.500000000	0.585780978
0.000000000	0.000000000	0.753552973
0.500000000	0.500000000	0.753552973
0.000000000	0.000000000	0.669615984
0.000000000	0.000000000	0.837450981
0.500000000	0.500000000	0.837450981
0.000000000	0.000000000	0.917414010
0.500000000	0.500000000	0.917414010
0.500000000	0.500000000	0.669615984
0.500000000	0.000000000	0.043048002
0.500000000	0.000000000	0.377903998
0.000000000	0.500000000	0.043048002
0.000000000	0.500000000	0.377903998
0.000000000	0.500000000	0.126725003
0.000000000	0.500000000	0.461326003
0.500000000	0.000000000	0.126725003
0.500000000	0.000000000	0.461326003
0.500000000	0.000000000	0.210721999
0.500000000	0.000000000	0.544968009
0.000000000	0.500000000	0.210721999
0.000000000	0.500000000	0.544968009
0.500000000	0.000000000	0.294349015
0.500000000	0.000000000	0.628823996
0.000000000	0.500000000	0.294349015

0.000000000	0.500000000	0.628823996
0.500000000	0.000000000	0.712791026
0.000000000	0.500000000	0.712791026
0.000000000	0.500000000	0.796814978
0.500000000	0.000000000	0.796814978
0.500000000	0.000000000	0.878480971
0.000000000	0.500000000	0.878480971
0.500000000	0.000000000	0.959644973
0.000000000	0.500000000	0.959644973
0.250000000	0.250000000	0.039781000
0.250000000	0.250000000	0.374704987
0.250000000	0.250000000	0.709504008
0.250000000	0.250000000	0.207451999
0.250000000	0.250000000	0.541786015
0.230000004	0.230000004	0.875850976
0.250000000	0.250000000	0.123420000
0.250000000	0.250000000	0.458117008
0.270000011	0.270000011	0.793416977
0.250000000	0.250000000	0.291106999
0.250000000	0.250000000	0.625606000
0.270000011	0.270000011	0.956925988
0.250000000	0.750000000	0.039781000
0.250000000	0.750000000	0.374704987
0.250000000	0.750000000	0.709504008
0.250000000	0.750000000	0.207451999
0.250000000	0.750000000	0.541786015
0.270000011	0.730000019	0.875850976
0.250000000	0.750000000	0.123420000

0.250000000	0.750000000	0.458117008
0.230000004	0.769999981	0.793416977
0.250000000	0.750000000	0.291106999
0.250000000	0.750000000	0.625606000
0.230000004	0.769999981	0.956925988
0.750000000	0.250000000	0.039781000
0.750000000	0.250000000	0.374704987
0.750000000	0.250000000	0.709504008
0.750000000	0.250000000	0.207451999
0.750000000	0.250000000	0.541786015
0.730000019	0.270000011	0.875850976
0.750000000	0.250000000	0.123420000
0.750000000	0.250000000	0.458117008
0.769999981	0.230000004	0.793416977
0.750000000	0.250000000	0.291106999
0.750000000	0.250000000	0.625606000
0.769999981	0.230000004	0.956925988
0.750000000	0.750000000	0.039781000
0.750000000	0.750000000	0.374704987
0.750000000	0.750000000	0.709504008
0.750000000	0.750000000	0.207451999
0.750000000	0.750000000	0.541786015
0.769999981	0.769999981	0.875850976
0.750000000	0.750000000	0.123420000
0.750000000	0.750000000	0.458117008
0.730000019	0.730000019	0.793416977
0.750000000	0.750000000	0.291106999
0.750000000	0.750000000	0.625606000

0.730000019	0.730000019	0.956925988
0.500000000	0.000000000	0.332309008
0.519999981	0.000000000	0.666912019
0.509999990	0.000000000	0.996056974
0.500000000	0.000000000	0.164757997
0.500000000	0.000000000	0.499305010
0.519999981	0.000000000	0.835112989
0.000000000	0.500000000	0.332309008
0.000000000	0.479999989	0.666912019
0.000000000	0.519999981	0.996056974
0.000000000	0.500000000	0.164757997
0.000000000	0.500000000	0.499305010
0.000000000	0.519999981	0.835112989
0.500000000	0.000000000	0.080863997
0.500000000	0.000000000	0.415861011
0.479999989	0.000000000	0.750856996
0.500000000	0.000000000	0.248683006
0.500000000	0.000000000	0.583028018
0.479999989	0.000000000	0.915111005
0.000000000	0.500000000	0.080863997
0.000000000	0.500000000	0.415861011
0.000000000	0.519999981	0.750856996
0.000000000	0.500000000	0.248683006
0.000000000	0.500000000	0.583028018
0.000000000	0.519999981	0.915111005

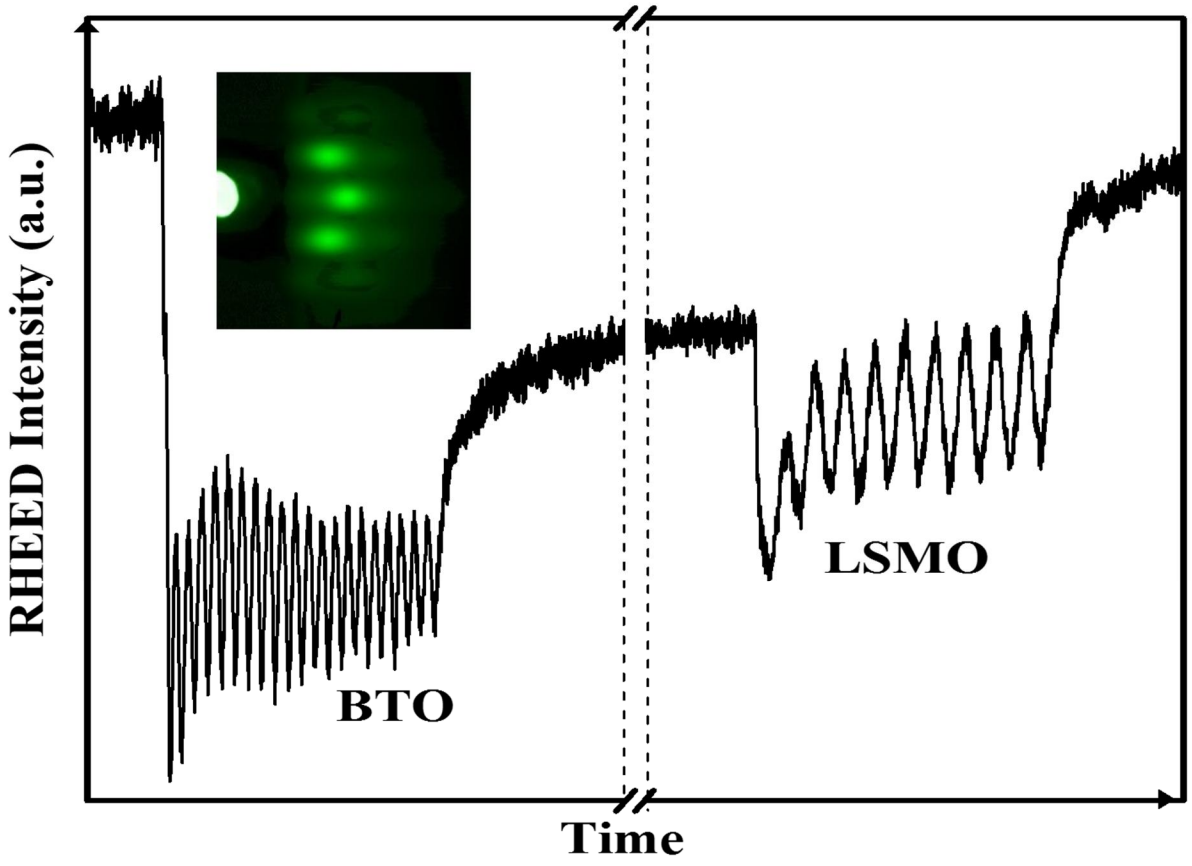

Fig. S1. RHEED oscillation and (inset) the final RHEED pattern of superlattice growth.

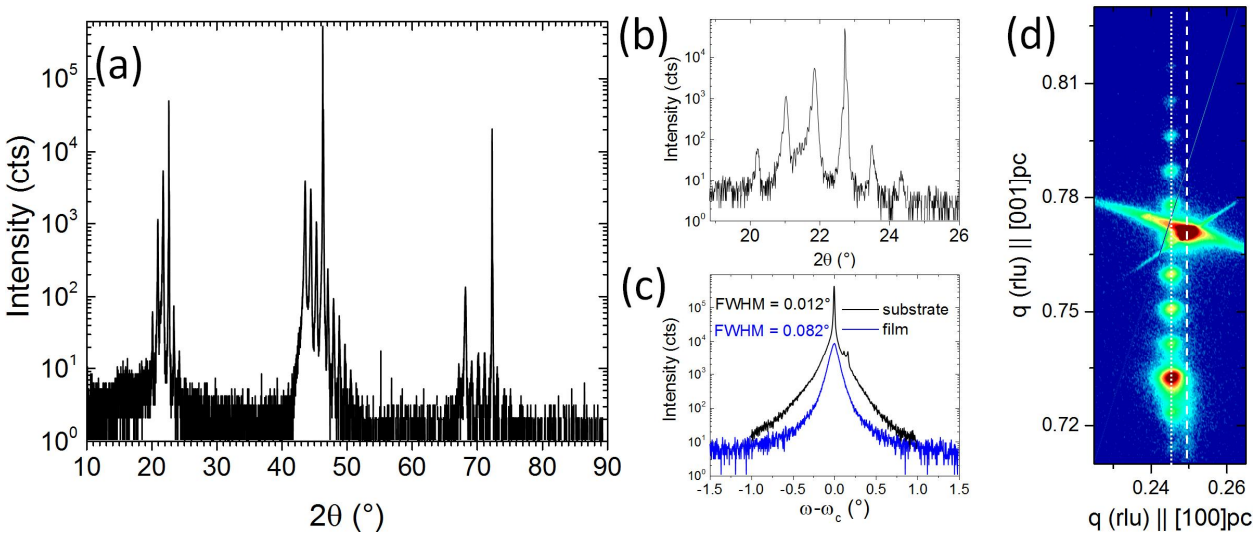

Fig. S2. X-ray diffraction data on $(BTO_{21}/LSMO_4)_{10}$. a) θ-2θ Scans through the (001)pc, (002)pc, and (003)pc peaks. b) Region near the (001) peaks show clear superlattice and Laue fringes. c) Rocking curve on the 002 BTO film and STO substrate reflections. d) Reciprocal-space mesh scan along the (103)pc axis shows that the BTO and LSMO layers have relaxed off the substrate but maintain internal epitaxy to each other.

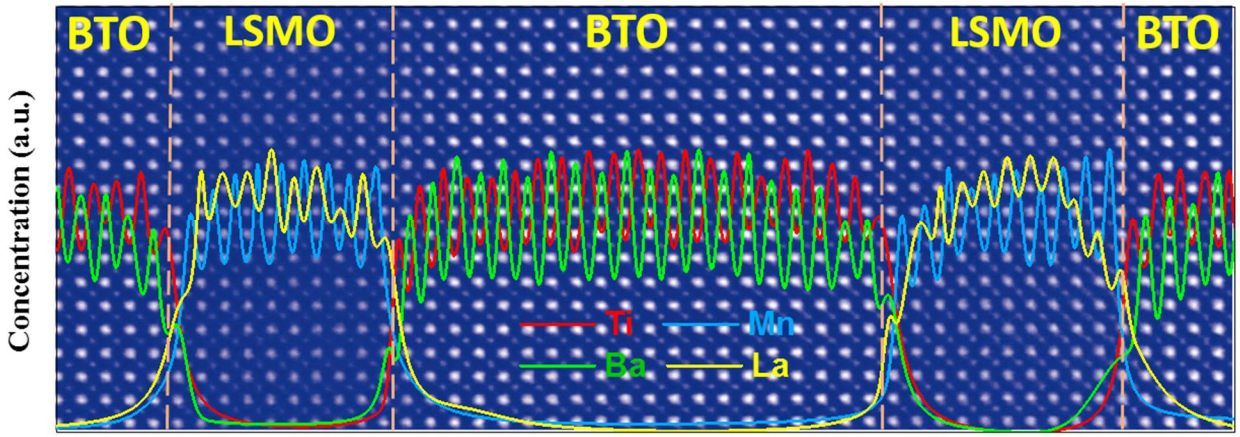

Fig. S3. HAADF-STEM image and EELS elemental profiles of BTO/LSMO N = 10 u.c. superlattice on (001)-oriented STO substrate taken along [100] direction. The dashed yellow lines mark the interfaces.

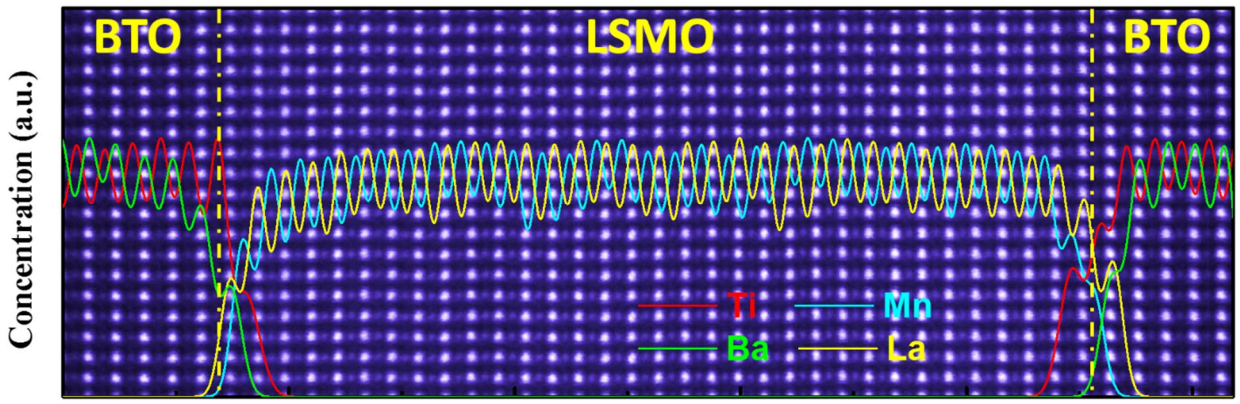

Fig. S4. HAADF-STEM image and EELS elemental profiles of BTO/LSMO N = 32 u.c. superlattice on (001)-oriented STO substrate taken along [110] direction. The dashed yellow lines mark the interfaces.

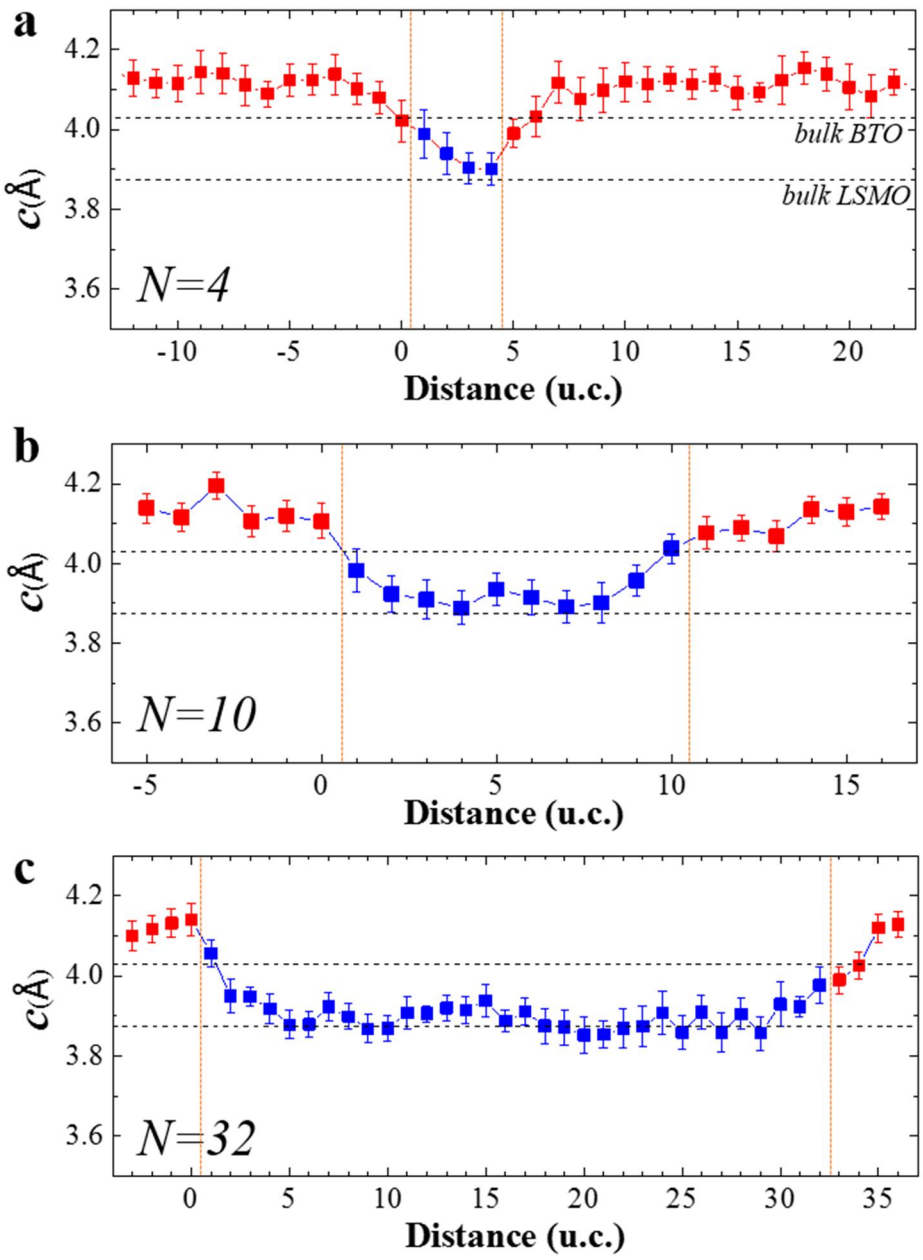

Fig. S5. Out-of-plane lattice constant of LSMO (blue dots) and BTO (red dots) for samples with (a) $N = 4$, (b) $N = 10$ and (c) $N = 32$ u.c. The dotted line indicates the c-axis lattice constant for bulk BTO (c = 4.03Å) and LSMO (c = 3.875 Å) for reference.

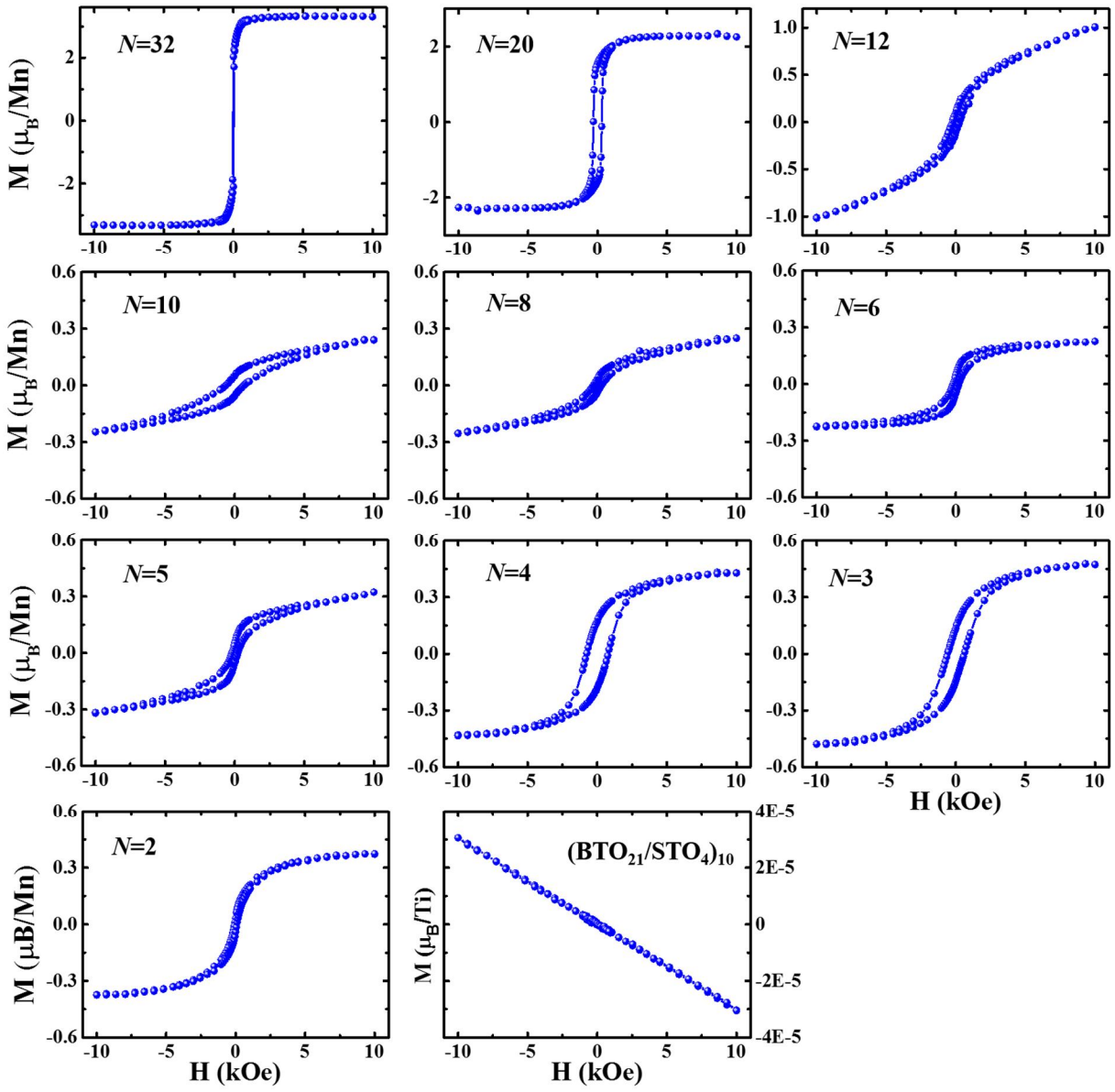

Fig. S6. *M* vs. *H* data taken at 10K for different LSMO thicknesses *N*. The bottom middle is a superlattice of BTO/STO showing that our BTO films only possess negligible diamagnetic signal.

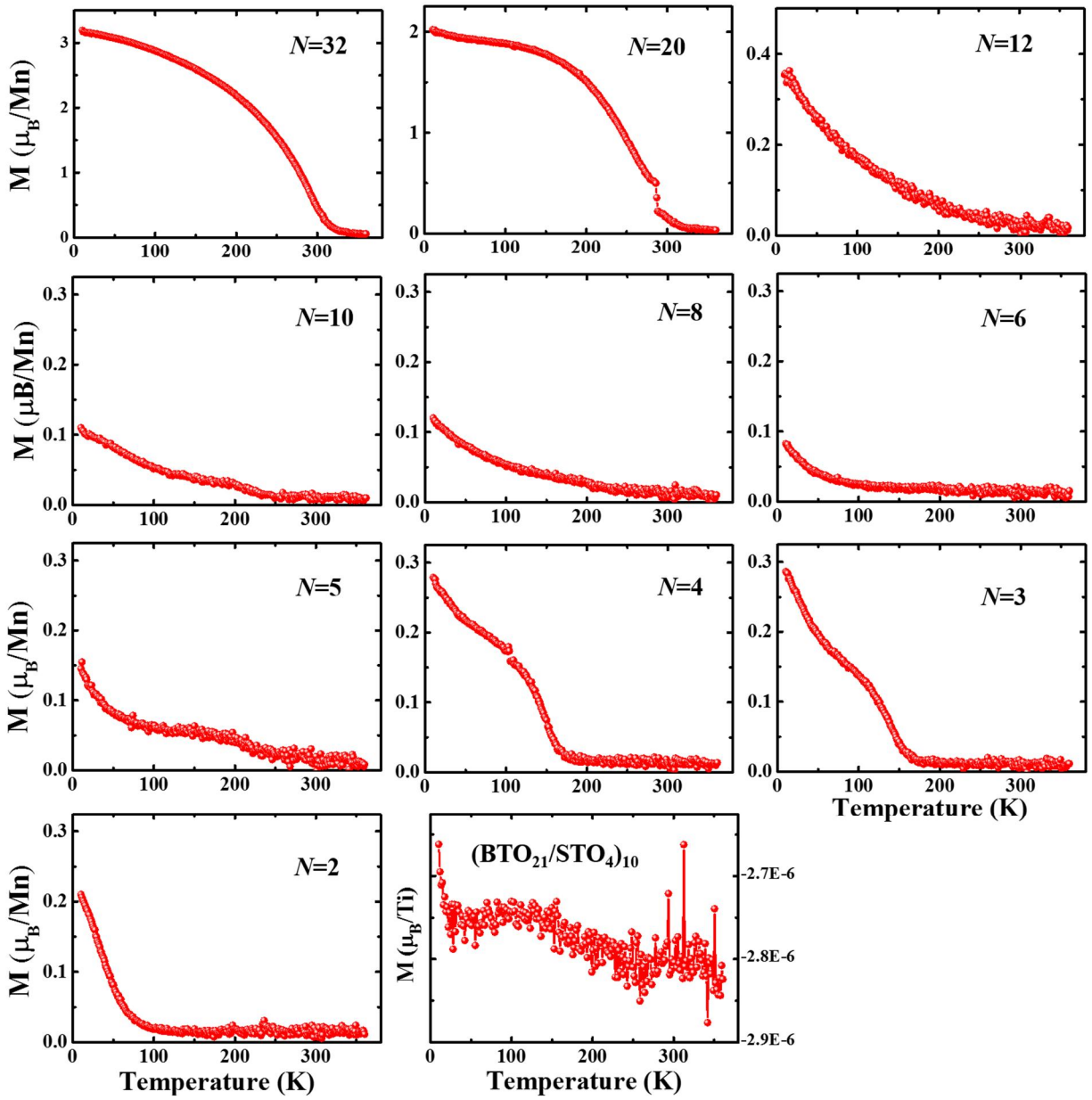

Fig. S7. *M* vs. *T* data at 1000 Oe for different LSMO thicknesses *N,* field cooled with 1T. The bottom middle is a superlattice of BTO/STO showing that our BTO films only possess negligible diamagnetic signal.

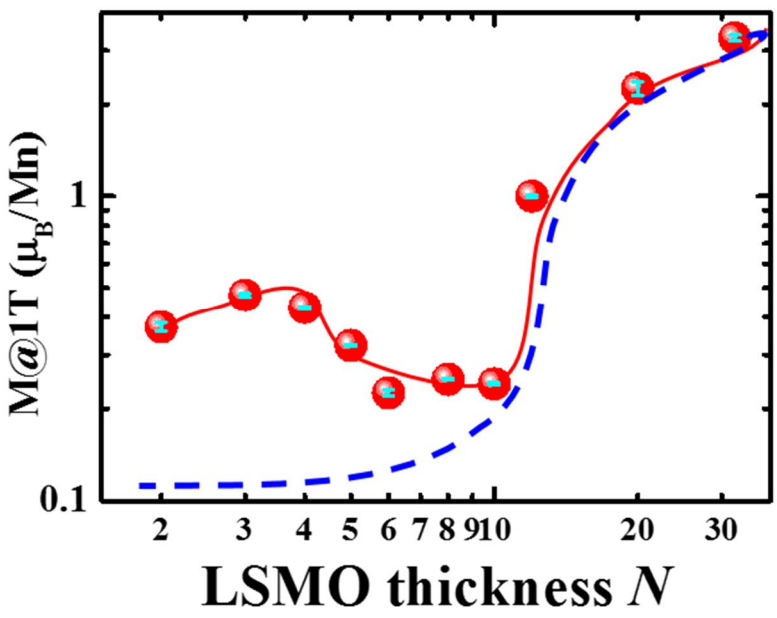

Fig. S8. Magnetic moment at 1T extracted from *M-H* curves in supplementary Fig. 2 for different LSMO thicknesses *N*. Error bar is embedded in cyan. Red curves are for eye guidance only. Blue dashed line are for eye guidance only indicating the monotonic decrease of magnetization in normal circumstances.

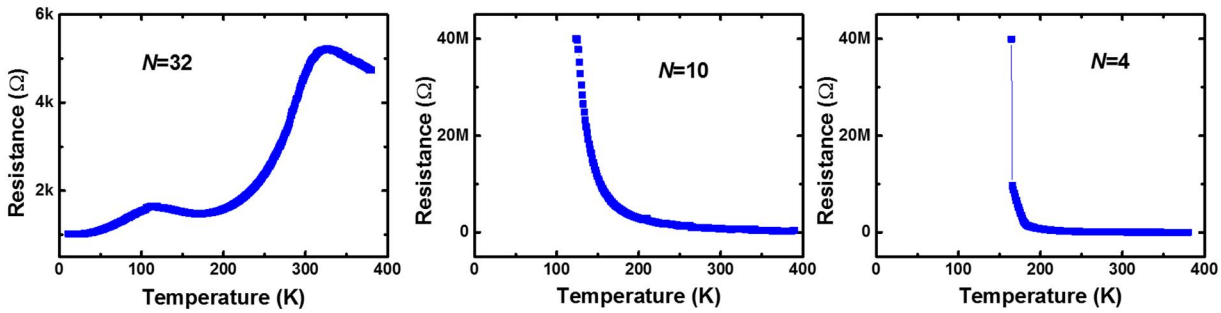

Fig. S9: Resistance vs Temperature for three superlattices in the manuscript. Note that for *N*=10 and 4 uc films at low temperatures, the resistance is too large and exceeds our measurement limit.

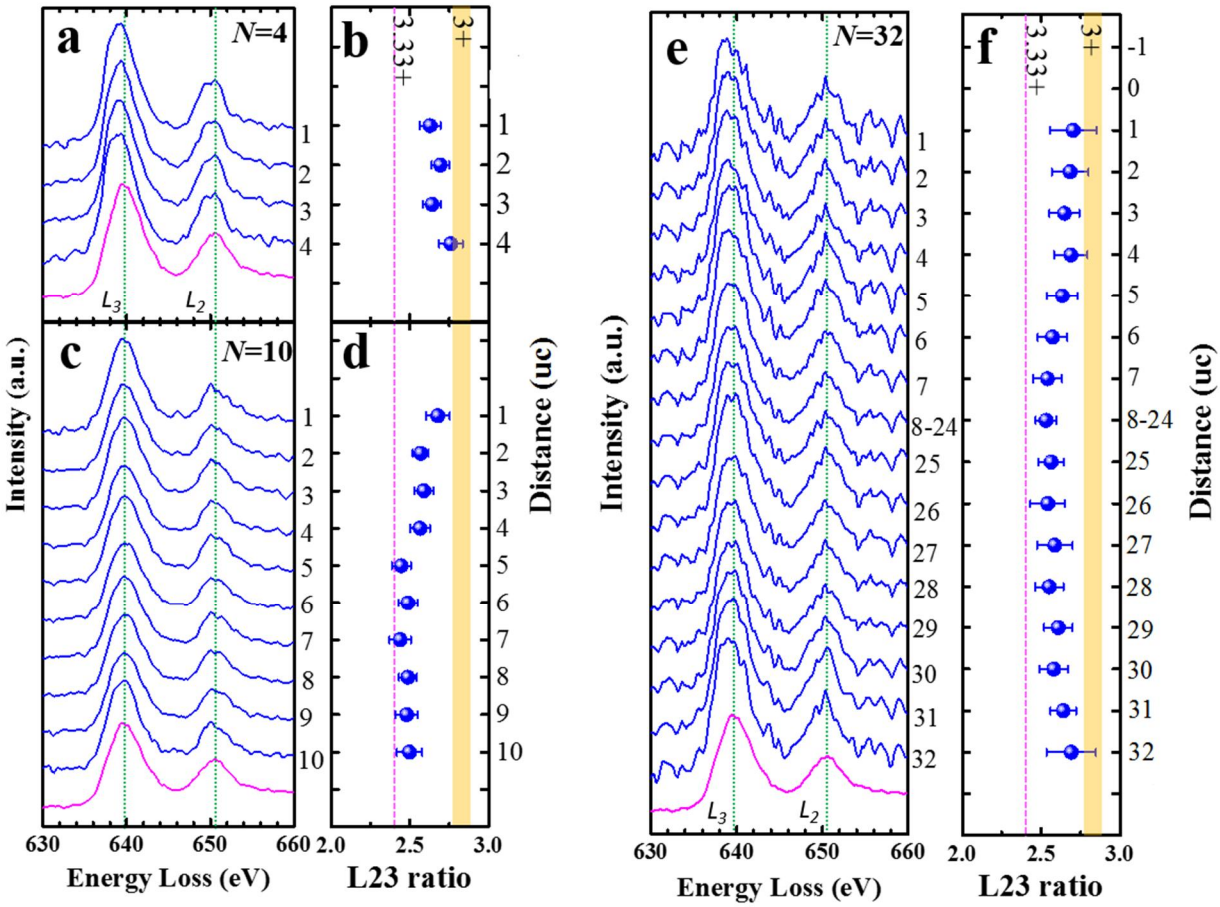

Fig. S10. Mn oxidation state for BTO/LSMO superlattice with $N = 4$, 10 and 32 u.c., determined from Mn L_{23} ratio. Background subtracted EELS spectra for Mn L edges for (a) $N = 4$ (c) $N = 10$ and (e) $N = 32$ u.c. LSMO are collected from every MnO_2 layer/unit cell starting from the left BTO/LSMO interface. An averaged spectrum from layer 8 to 24 presents the feature of Mn in the middle of the $N = 32$ u.c. sample. (b, c, f) The corresponding Mn L_{23} ratio calculated from the EELS spectra using Hartree-Slater cross-section step functions as a function of unit cell. The error bar is estimated based on the deviation of the substrate. The yellow band and the blue line indicate the position of Mn^{3+} and $Mn^{3.33+}$.

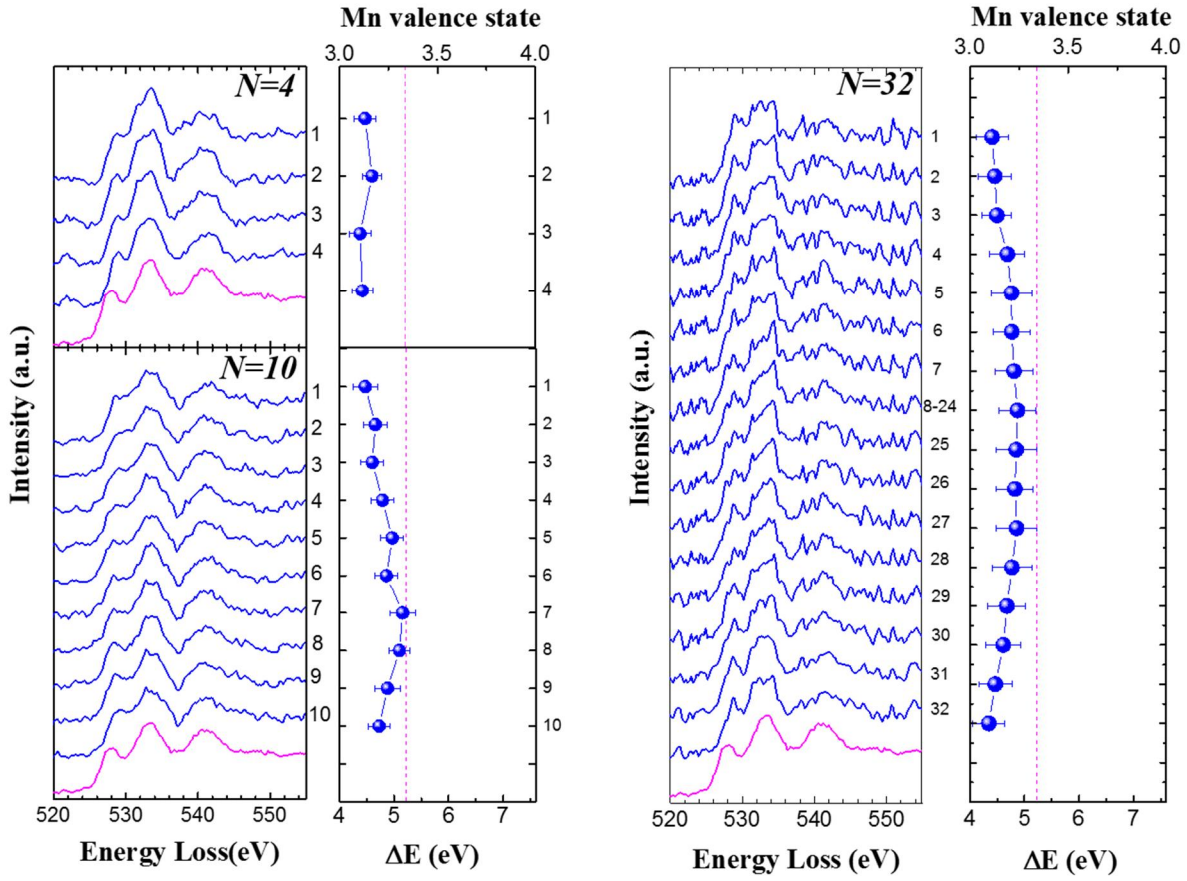

Fig. S11. Mn oxidation state for BTO/LSMO superlattice with $N = 4$, 10 and 32 u.c. determined by O-*K* edge. Background subtracted EELS spectra for O-*K* edge for (a) $N = 4$ (c) $N = 10$ and (e) $N = 32$ u.c. LSMO is collected from every MnO_2 layer starting from the left BTO/LSMO interface. An averaged spectrum from 8 uc to 24 uc presenting the feature of Mn L edges in the middle of $N = 32$ u.c. sample. (b, d, f) The energy separation between pre-peak and main peak calculated from the EELS spectra as a function of unit cell.

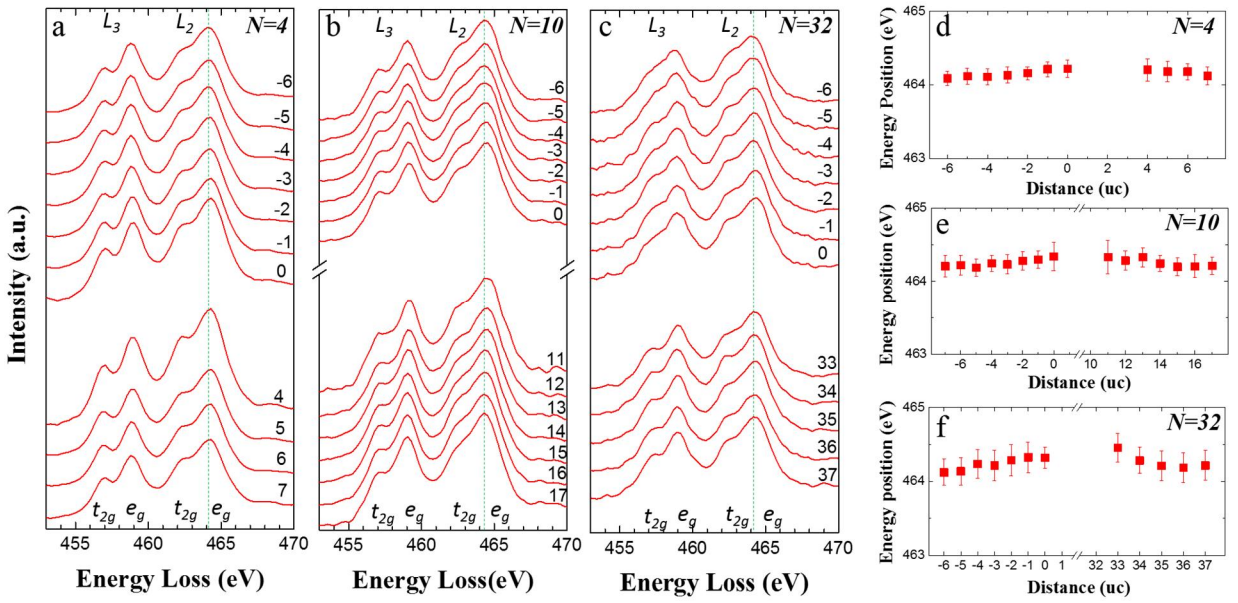

Fig. S12. Ti oxidation state for BTO/LSMO superlattice with $N = 4$, 10 and 32 u.c. Background subtracted EELS spectra for Ti-$L_{2,3}$ edge for samples with (a) $N = 4$, (b) $N = 10$ and (c) $N = 32$ u.c. The termination TiO_2 layer of the left-side BTO/LSMO interface was set as $x = 0$. (d-f) The energy position of the L_3 e_g peaks as a distance from the interface was measured from the spectra. The redshift of the L_3 edges near the BTO/LSMO and LSMO/BTO interfaces indicate a slight increase of Ti valence state about +0.1.

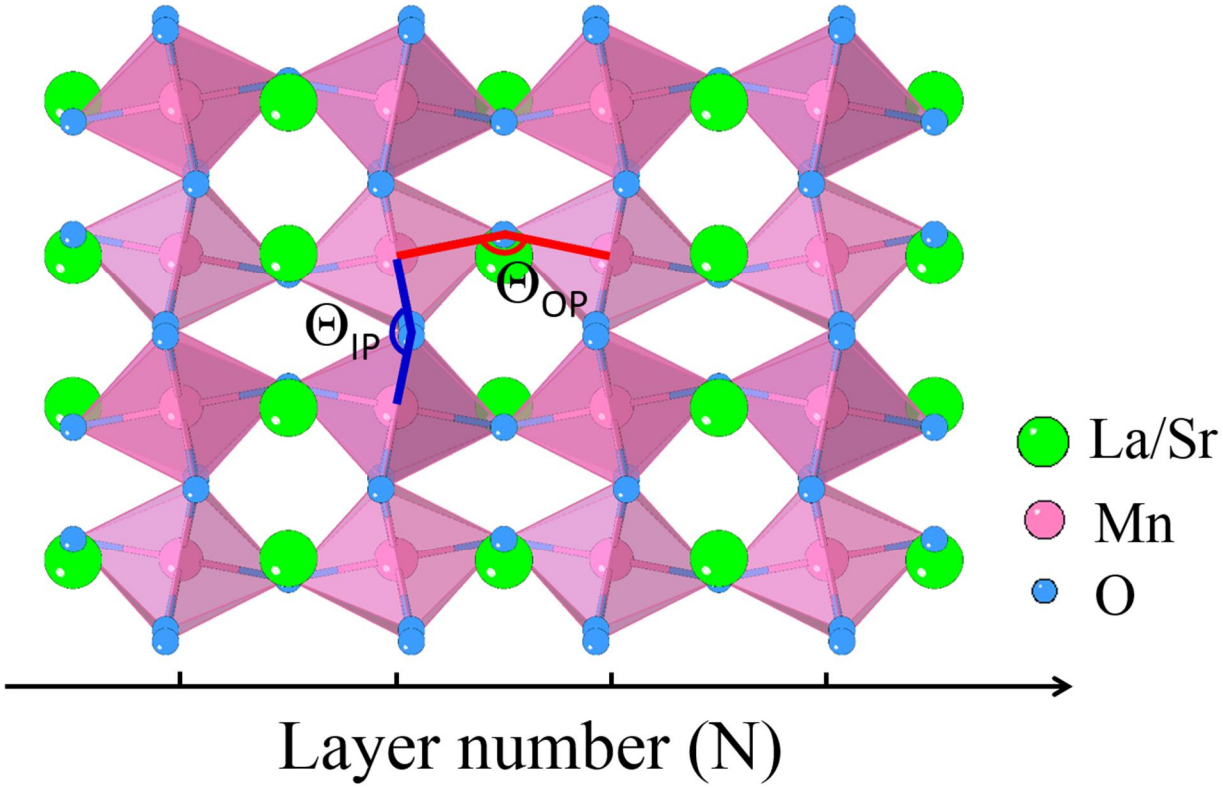

Fig. S13. Rigid structure model of LSMO along [110] direction. Blue and red marks represent in-plane (IP) and out-of-plane (OP) Mn-O-Mn bonds, respectively.

References

1. Varela M, et al. (2009) Atomic-resolution imaging of oxidation states in manganites. *Phys Rev B* 79(8): 085117.
2. Dagotto E (2002) Nanoscale Phase Separation and Colossal Magnetoresistance. Berlin: Springer.
3. Dagotto E, Hotta T, Moreo A (2001) Colossal magnetoresistant materials: The key role of phase separation. *Phys Rep* 344: 1-135.
4. Slater JC, Koster GF (1954) Simplified LCAO method for the periodic potential problem. *Phys Rev* 94(6): 1498.
5. Sergienko IA, Sén C, Dagotto E (2006) Ferroelectricity in the magnetic E-phase of orthorhombic perovskites. *Phys Rev Lett* 97(22): 227204.
6. Zhou JS, Goodenough JB (2008) Intrinsic structural distortion in orthorhombic perovskite oxides. *Phys Rev B* 77(13): 132104.
7. Dong S et al. (2012) Magnetic and orbital order in $(RMnO_3)_n/(AMnO_3)_{2n}$ superlattices studied via a double-exchange model with strain. *Phys Rev B* 86(20): 205121.
8. Dong S, Yu R, Liu JM, Dagotto E (2009) Striped multiferroic phase in double-exchange model for quarter-doped manganites. *Phys Rev Lett* 103(10): 107204.